

# PastNet: Introducing Physical Inductive Biases for Spatio-temporal Video Prediction

Hao Wu  
School of Computer Science and  
Technology, University of Science and  
Technology of China  
Hefei, China  
wuhao2022@mail.ustc.edu.cn

Wei Xiong  
Department of Earth System Science,  
Tsinghua University  
Beijing, China  
xiongw21@mails.tsinghua.edu.cn

Fan Xu  
School of Computer Science and  
Technology, University of Science and  
Technology of China  
Hefei, China  
markxu@mail.ustc.edu.cn

Xiao Luo  
Department of Computer Science,  
University of California  
Los Angeles, USA  
xiaoluo@cs.ucla.edu

Chong Chen  
Terminus Group  
Beijing, China  
cheung1990@126.com

Xian-Sheng Hua  
Terminus Group  
Beijing, China  
huaxiansheng@gmail.com

Haixin Wang  
National Engineering Research  
Center for Software Engineering,  
Peking University  
Beijing, China  
wang.hx@stu.pku.edu.cn

## ABSTRACT

In this paper, we investigate the challenge of spatio-temporal video prediction, which involves generating future videos based on historical data streams. Existing approaches typically utilize external information such as semantic maps to enhance video prediction, which often neglect the inherent physical knowledge embedded within videos. Furthermore, their high computational demands could impede their applications for high-resolution videos. To address these constraints, we introduce a novel approach called Physics-assisted Spatio-temporal Network (PastNet) for generating high-quality video prediction. The core of our PastNet lies in incorporating a spectral convolution operator in the Fourier domain, which efficiently introduces inductive biases from the underlying physical laws. Additionally, we employ a memory bank with the estimated intrinsic dimensionality to discretize local features during the processing of complex spatio-temporal signals, thereby reducing computational costs and facilitating efficient high-resolution video prediction. Extensive experiments on various widely-used datasets demonstrate the effectiveness and efficiency of the proposed PastNet compared with a range of state-of-the-art methods, particularly in high-resolution scenarios. Our code is available at <https://github.com/easylearningscores/PastNet>.

## CCS CONCEPTS

• **Computing methodologies** → *Scene understanding*.

## KEYWORDS

Spatiotemporal predictive learning, Physical Inductive Biases, high-resolution video prediction

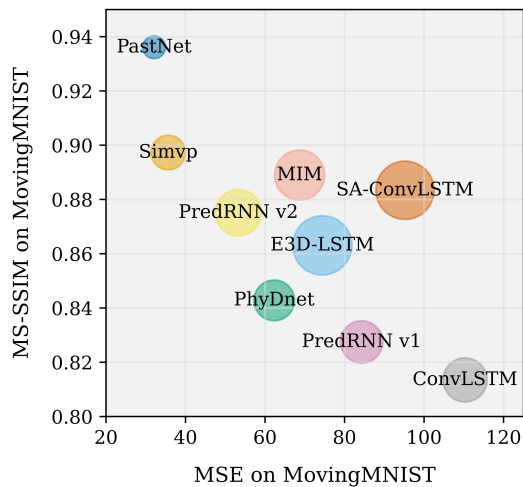


**Figure 1: Performance comparison of different video prediction methods on MovingMNIST. Our PastNet outperforms previous models in terms of training time and image quality. Specifically, the PastNet achieves the lowest MSE and highest MS-SSIM scores when trained for 100 epochs, and its training time is remarkably shorter than other models. The small bubble of the PastNet indicates that it consumes the least amount of time during training.**

## 1 INTRODUCTION

Spatial-temporal forecasting has emerged as a significant area of interest within the multimedia research community [8, 26, 53, 58]. Among numerous practical problems, the objective of video prediction is to generate future video frames by leveraging historical

frames [7, 49]. This problem bears considerable relevance to an array of applications, including human motion prediction [1], climate change analysis [39], and traffic flow forecasting [48].

In literature, a multitude of methods have been devised for efficacious video prediction, integrating deep neural networks to capture complex correlations within spatio-temporal signals [5]. Early approaches [29, 39, 44, 51] amalgamate convolutional neural networks (CNNs) and recurrent neural networks (RNNs) to extract features from RGB frames and predict future trends, respectively. Several techniques also employ deep stochastic models to generate video prediction while taking into account diverse potential results [1, 13, 43, 52, 53]. More recently, a range of algorithms has sought to enhance video prediction by incorporating external information such as optical flow, semantic maps, and human posture data [22, 27, 32, 45]. For example, SADM [2] combines semantic maps with flow fields to supply contextual information exhibiting superior compatibility. Nevertheless, these external inputs could not be readily available in practical situations [20, 32, 50]. In light of this consideration, a recent study [14] demonstrates that a basic CNN-based model can achieve state-of-the-art performance through end-to-end optimization.

Despite their remarkable achievements, the performance of existing approaches remains far from satisfactory for the following reasons: (1) **Neglect of Underlying Physical Principles.** Current methods typically employ deep neural networks to extract information from spatial space and the associated visual domains [14, 22, 27, 45]. However, video frames could be governed by underlying physical principles, such as partial differential equations (PDEs) [16, 28, 34]. For instance, climate videos are typically dominated by high-order equations. As a consequence, it is anticipated to explore these physical principles for effective video prediction. (2) **Low Efficiency.** As a dense prediction problem [36], the scalability of neural network models is critical for high-resolution video prediction [5]. Regrettably, the majority of existing models rely on complex neural networks, such as deep CNNs and Vision Transformers [37, 56], which entail significant computational costs and render them unsuitable for large-scale high-resolution videos.

To address these concerns, this paper introduces a novel approach called Physics-assisted Spatio-temporal Network (PastNet) for high-quality video prediction. The core of our PastNet is to introduce inductive physical bias using the data itself, which holds the potential to solve underlying PDEs. Specifically, we introduce a convolution operator in the spectral space that initially transfers video frames into the Fourier domain, followed by efficient parallelizable channel fusion [17]. Subsequently, we employ an inverse Fourier transform to generate the outputs. Furthermore, to enhance efficiency for high-resolution video implementation, our PastNet introduces a discrete spatio-temporal module, which not only estimates intrinsic dimensionality but also introduces memory banks to discretize local features during the processing of complex spatio-temporal signals, replacing local features with their nearest queries from the memory bank. Finally, a deconvolution decoder is incorporated to output the predictions, which are combined with outputs from the spectral space. Comprehensive experiments on various benchmark datasets substantiate the effectiveness and efficiency of our proposed PastNet. A glimpse of the compared results by various approaches is provided in Figure 1 and we can observe

the huge superiority of our PastNet on MovingMNIST. Our main contributions can be summarized as follows:

- **New Perspective.** We open up a new perspective to connect spatio-temporal video prediction with physical inductive biases, thereby enhancing the model with data itself.
- **Novel Methodology.** Our PastNet not only employs a convolution operator in the spectral space to incorporate physical prior but also discretizes local features using a memory bank with the estimated intrinsic dimensionality to boost efficiency for high-resolution video prediction.
- **High Performance and Efficiency.** Comprehensive experiments on a variety of datasets demonstrate that the PastNet exhibits competitive performance in terms of both effectiveness and efficiency.

## 2 RELATED WORK

### 2.1 Spatio-temporal Video Prediction

Video prediction has emerged as an essential topic within the multimedia research community, and numerous methods have been proposed to address this challenge. Initial studies frequently examine spatio-temporal signals extracted from RGB frames [29, 39, 44, 47, 51]. For instance, ConvLSTM [39] employs convolutional neural networks (CNNs) to encode spatial data, which is subsequently integrated with an LSTM model to capture temporal dependencies. PredNet [29] draws inspiration from neuroscience, enabling each layer to make local predictions for video sequences. MCnet [44] introduces multiple pathways to encode motion and content independently, which are combined into an end-to-end framework. Various approaches strive to merge video prediction with external information from optical flow, semantic maps and human posture data [22, 27, 32, 45]. As a representative unsupervised method, DVF [27] predicts missing frames using masked ones. HVP [22] treats this problem as video-to-video translation from semantic structures, inspired by hierarchical models. SADM [2] combines semantic maps and flow fields to provide more compatible contextual information. However, this external information could be inaccessible in real-world applications [20, 32, 50]. Furthermore, the efficiency and effectiveness of current solutions remain suboptimal for high-resolution videos. To surmount these obstacles, we propose a novel method that incorporates both physical inductive biases and quantization operations for high-quality video prediction.

### 2.2 Physics-Informed Machine Learning

Various machine learning problems can benefit from the incorporation of physical knowledge [21]. Modern physics-informed machine learning approaches can leverage knowledge from three aspects, i.e., observational biases, inductive biases, and learning biases. Observational biases primarily arise from the data itself [24, 30, 55], offering a range of data augmentation strategies to expand datasets. Inductive biases guide the specific design of neural networks such as graph neural networks [3] and equivariant networks [9], which possess properties of respecting additional symmetry groups [3]. Learning biases pertain to the process of imposing distinct constraints by incorporating loss objectives during optimization [15], adhering to the principles of multi-task learning. For instance, physics-inspired

neural networks [35] (PINNs) typically include constraints related to derivatives from PDEs, resulting in superior performance in modeling dynamical systems and predicting molecular properties. To bolster predictive performance, our PastNet introduces inductive biases from the underlying PDEs of video frames by integrating learnable neural networks in the Fourier domain.

### 2.3 Data Compression

Compressing large-scale data is essential for enhancing the efficiency of both training and inference processes [31]. Learning to hash is a widely employed technique that accomplishes this by mapping continuous vectors to compact binary codes while preserving similarity relationships, which achieves extensive progress in approximate nearest neighbor search [4]. Another line to address this challenge is neural quantization. For instance, multi-codebook quantization [59] is akin to the process of k-means clustering, which stores centroids and assignments in the codebooks. Recently, VQ-VAE [41] has integrated neural quantization with auto-encoders, using discrete codes to reconstruct input images and leading to efficient models for large-scale applications. VQ-VAE has been successfully applied in various scenarios, including video generation [54], image inpainting [33], and semantic communication [19]. In this paper, our DST module is inspired by VQ-VAE, discretizing local features to improve efficiency in high-resolution video prediction.

## 3 METHODOLOGY

### 3.1 Overview

This paper studies the problem of spatio-temporal video prediction and existing solutions usually neglect underlying physical principles and suffer from larger computational space. To tackle this, our proposed PastNet introduces both *Fourier-based physics-guided (FPG) module* and *discrete spatio-temporal (DST) module* for effectively and efficiently video prediction as in Figure 2. In particular, our FPG module first divides frame into non-overlapping patches and then introduce a Fourier-based *priori* spectral filters with the introduction of physical inductive biases. Then, our DST module not only estimates intrinsic dimensionality but also introduces a discrete memory bank to effectively and efficiently capture spatio-temporal signals. Following is the problem definition and the detailed description of these key components of our proposed PastNet.

**Problem Definition.** To enhance clarity, we offer a comprehensive explanation of the relevant concepts. Assume a video trajectory represents a dynamic physical system in the temporal domain, consisting of  $T$  time steps, denoted as  $V_{1:T} = \{V_1, \dots, V_T\}$ . Each snapshot captures  $C$  color space measurements over time at all locations within a spatial region, represented by an  $H \times W$  grid. From a spatial viewpoint, the observation of these  $C$  measurements at any specific time step  $i$  can be depicted as a tensor,  $V_i \in \mathbb{R}^{C \times H \times W}$ . Our objective is to leverage spatio-temporal data to deduce underlying physical priors and integrate feature representation learning in both spatial and temporal dimensions and predict the most probable future sequence of length  $T_f$ , denoted as  $V_{T+1:T+T_f}^{fut} = \{V_{T+1}, \dots, V_{T+T_f}\}$ .

### 3.2 Fourier-based Physics-Guided (FPG) Module

Our primary insight focuses on utilizing prior physical signals to achieve effective spatio-temporal video prediction. In fact, spatio-temporal data is often subject to complex, high-dimensional non-linear physical equations (e.g., Navier-Stokes equation), which are challenging to capture. Inspired by previous studies [17, 24], we employ spectral methods and develop an algorithm that seamlessly combines trainable neural networks with Fourier-based *priori* spectral filters. It has been shown that the features transformed through Fourier transformation in the frequency domain correspond precisely with the coefficients of the underlying physical partial differential equation [18, 24]. As a result, we can utilize neural networks to approximate the analytical solution of the latent PDE. To be specific, we initially divide video frames into non-overlapping patches with initialized embeddings and subsequently transform them into a spectral space. The features within the frequency domain are fused, followed by an inverse transformation returning them to the spatial domain. This innovation supports a physical inductive bias derived from data, demonstrating significant potential for solving PDEs. Then, we introduce our FPG module in detail.

**Embedding Initialization.** Given the input video  $V \in \mathbb{R}^{T \times C \times H \times W}$ , we extract the high-level learnable representations following ViT [11]. In particular, we divide the frame into non-overlapping  $N = HW/hw$  patches of size  $h \times w$  and then project them into patch embeddings  $E^{pat} \in \mathbb{R}^{T \times h \times w \times d}$ , where  $d$  denotes the embedding dimension. Position embeddings  $E^{pos} \in \mathbb{R}^{h \times w \times d}$  are also applied to get the initial token representation matrix  $\hat{V} \in \mathbb{R}^{T \times h \times w \times d}$ . In formulation,

$$\hat{V}_t = E_t^{pat} + E^{pos}, \quad (1)$$

where  $\hat{V}_t = \hat{V}[t, :, :] \in \mathbb{R}^{h \times w \times d}$  makes up the matrix  $\hat{V}$ .

**Fourier-based Spectral Filter.** We apply  $\hat{V}$  as input to  $L$  layers of filters, each layer containing three essential components, i.e., *Fourier transform, separate mixing and inverse Fourier transform*. Firstly, a 2D fast Fourier transform (FFT) is leveraged to generate the frequency domain token  $\mathcal{K}_t \in \mathbb{R}^{h \times w \times d}$  at time step  $t$ :

$$\mathcal{K}_t(u, v) = \sum_{x=0}^{h-1} \sum_{y=0}^{w-1} \hat{V}_t(x, y) e^{-2\pi i (\frac{x}{h}u + \frac{y}{w}v)}, \quad (2)$$

where  $i$  is the imaginary unit, and  $u$  and  $v$  are the indices of rows and columns in the frequency domain, respectively.

Secondly, the complex-valued token  $\mathcal{K} = \mathcal{K}_{1:T}$  is then split into its real and imaginary parts and concatenated along the channel dimension. To enhance the integration of feature information, we utilize token mixing across different channels, which allows for richer Fourier mode representations to emerge through greater fusion of channel-wise signals. It is implemented with separate MLPs for the real and imaginary parts separately as follows:

$$\mathfrak{R}\hat{\mathcal{K}}_t(u, v) = \text{MLP}_{\theta_1}(\mathfrak{R}\mathcal{K}_t(u, v)), \quad \mathfrak{I}\hat{\mathcal{K}}_t(u, v) = \text{MLP}_{\theta_2}(\mathfrak{I}\mathcal{K}_t(u, v)), \quad (3)$$

where  $\mathfrak{R}$  and  $\mathfrak{I}$  denotes the operator to obtain the real part and imaginary part, respectively. Performing token mixing mixes different modes across the Fourier domain. As the Fourier domain possesses global attributes, it further explore long-range relationships for underlying physical features.

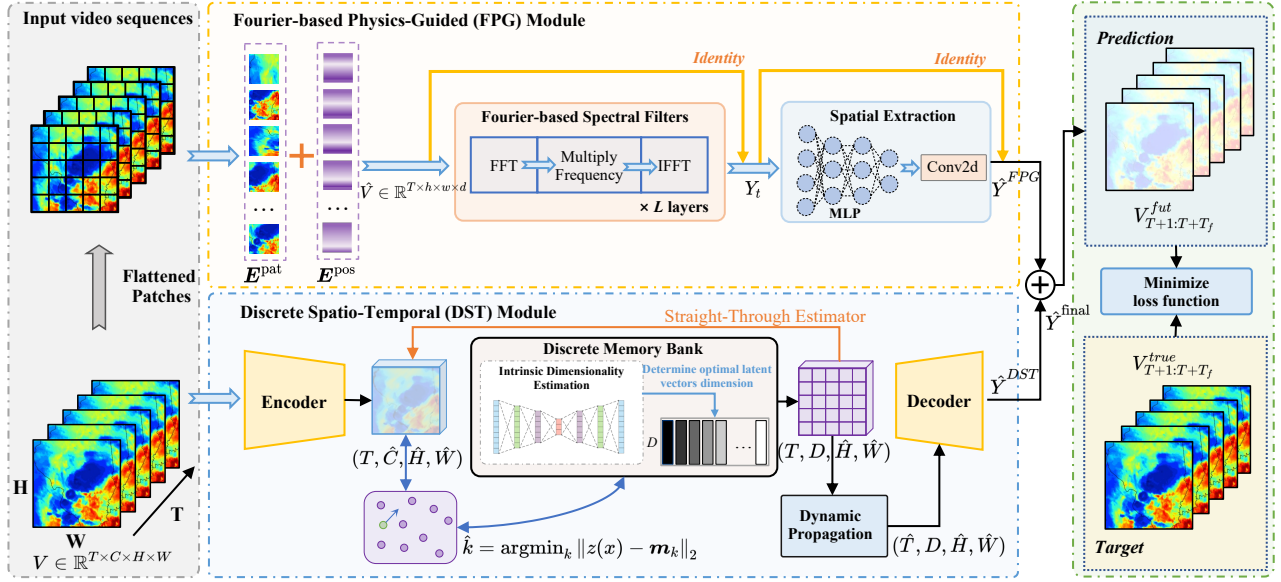


**Figure 2: An overview of the proposed PastNet, which consists of a Fourier-based Physics-guided (FPG) and a Discrete Spatio-temporal (DST) module. The PFI module first divides video frames into non-overlapping patches and introduce Fourier-based spectral filter with the introduction of physical biases. Then, its also extract spatial signals with convolutional neural networks. The DST module is an encoder-decoder architecture, which introduces a memory bank to discretize local features in estimated intrinsic dimensionality.**

Lastly, the mixed tokens are then transformed back to the spatial domain using the 2D inverse Fourier transform to obtain the output of spectral filter layers  $Y \in \mathbb{R}^{T \times h \times w \times d}$  as follows:

$$Y_t(x, y) = \frac{1}{hw} \sum_{u=0}^{h-1} \sum_{v=0}^{\frac{w}{2}} \hat{\mathcal{K}}_t(u, v) e^{2\pi i(\frac{u}{h}x + \frac{v}{w}y)} + \frac{1}{hw} \sum_{u=0}^{h-1} \sum_{v=\frac{w}{2}+1}^{w-1} \hat{\mathcal{K}}_t(u, v) e^{2\pi i(\frac{u}{h}x + \frac{v-w}{w}y)}, \quad (4)$$

where  $Y_t = Y[t, :, :] \in \mathbb{R}^{N \times M}$  makes up the matrix  $Y$ .

**Spatial Extraction.** To better extract the latent spatial information, we introduce classic convolutional neural networks as a supplement of the *priori* spectral filters, which can be formulated as follows:

$$\hat{Y}_t^{FPG} = \text{Tanh}(\text{Conv2d}(\text{MLP}(Y_t) + Y_t)), \quad (5)$$

The convolutional layer is known for its ability to extract features in the spatial domain through its local receptive fields. By leveraging these learned features as filters in the frequency domain, the convolutional layer can effectively mine potential physical information from the input data. The extracted physical information can significantly enhance the performance of spatiotemporal prediction.

Overall, the Fourier-based physics-guided module transforms the spatial domain of latent physical information into the frequency domain using Fourier transforms, and learns the analytical solutions of PDEs using neural networks. This approach allows PastNet to handle complex geometries and high-dimensional problems.

### 3.3 Discrete Spatio-temporal (DST) Module

Our discrete spatio-temporal (DST) module aims to explore spatio-temporal signals in video frames in an efficient manner. To achieve this, we not only estimate the intrinsic dimensionality for the hidden space, but also introduces a memory bank to vector quantization. In particular, it consists of four different modules, i.e., *encoder*, *intrinsic dimensionality estimation*, *discrete quantization*, *dynamic propagation* and *decoder*. Then, we introduce them in detail.

**Encoder.** The encoder contains  $K_e$  ConvNormReLU blocks to capture spatial signals. Given  $Z^{(0)} = V$  and an activation function  $\sigma$ , we have:

$$Z^{(i)} = \sigma \left( \text{LayerNorm} \left( \text{Conv2d} \left( Z^{(i-1)} \right) \right) \right), 1 \leq i \leq K_e, \quad (6)$$

where  $Z^{(i-1)}$  and  $Z^{(i)}$  denote the input and output of the  $i$ -th block with the shapes  $(T, C, H, W)$  and  $(T, \hat{C}, \hat{H}, \hat{W})$ , respectively.

**Intrinsic Dimensionality Estimation.** How to decide the dimensionality of the hidden space remains a challenging problem [6]. In particular, too large dimensionality would bring in redundant computational time and potential overfitting while too small one would underfit data. Here, we turn to Levina-Bickel algorithm [23] to acquire intrinsic dimensionality.

In particular, we start with a large dimensionality followed by mapping  $Z^{(K_e)}$  back to the input using a decoder and minimize the reconstruction loss objective as  $L_{rec} = \|V - \hat{V}\|$  where  $\hat{V}$  is the reconstructed frame. Then, we identify the  $R$  nearest neighbours for each vector  $h_j \in Z^{(K_e)}$ , i.e.,  $\{h_{j_1}, \dots, h_{j_R}\}$  and calculate the

local estimator for the vector as:

$$D_j = \frac{1}{R-2} \sum_{m=1}^{R-1} \log \frac{d(\mathbf{h}_j, \mathbf{h}_{jR})}{d(\mathbf{h}_j, \mathbf{h}_{jm})}, \quad (7)$$

where  $d(\cdot, \cdot)$  denotes the cosine distance between two vectors. Finally, we take the average all local estimators to generate the final estimator:

$$D = \frac{1}{J} \sum_{j=1}^J D_j, \quad (8)$$

where  $J$  is the number of vectors in  $Z^{(K_e)}$  and  $\cdot$  denotes the ceiling function. After generating final estimated optimal dimension, we utilize  $D$  as the hidden embedding instead.

**Discrete Quantization.** Previous methods usually process video features directly using spatio-temporal convolution modules. However, directly feeding video features into these modules would bring in huge computational cost. Therefore, we introduce a discrete memory bank to discretize feature vectors, which are constructed by a variational autoencoder [41, 54]. In this way, computational costs can be largely reduced to fit for large-scale video prediction.

In detail, we initialize the memory bank with variational autoencoder. Here, each embedding vector  $z$  from  $Z^{(K_e)}$  from the output of the encoder is mapped to the nearest point in the memory bank. The number of embeddings in the memory is set to  $D^2$  empirically. Given the memory bank with  $D^2$  embedding vectors,  $\{\mathbf{m}_1, \dots, \mathbf{m}_{D^2}\}$ , we construct a mapping  $VQ$ :

$$VQ(z) = \mathbf{m}_{\hat{k}}, \quad \text{where } \hat{k} = \operatorname{argmin}_k \|z(x) - \mathbf{m}_k\|_2, \quad (9)$$

where each embedding  $z$  is concatenated to generate matrix  $\bar{Z} = VQ(Z^{(K_e)})$ . The mapping connects continuous vectors with given vectors in the memory bank to save the computational cost. Then, to minimize the information loss, we map the concatenated matrix back to the input using a new decoder, i.e.,  $\tilde{V} = \operatorname{Dec}(\bar{Z})$ . The whole framework is optimized using the following objective as:

$$\mathcal{L} = \|\mathbf{V} - \tilde{\mathbf{V}}\| + \left\| \operatorname{sg}[\bar{Z}] - Z^{(K_e)} \right\|_2^2 + \beta \left\| \bar{Z} - \operatorname{sg}[Z^{(K_e)}] \right\|_2^2, \quad (10)$$

where  $\beta$  denotes a parameter to balance these objective and  $\operatorname{sg}(\cdot)$  is the stopgradient operator to cut off the gradient computation during back propagation. Here, the first term denotes the reconstruction loss and the last two terms minimize the quantization loss between continuous embedding vectors and their neighbours in the memory bank.

**Dynamic Propagation.** After training the variational autoencoder, we remove the decoder, and then feed the quantized vector into temporal convolution on  $T \times D$  channels. In particular, each temporal convolution block involves a bottleneck followed by group convolution operator:

$$Z^{(i)} = \operatorname{GroupConv2d}(\operatorname{Bottleneck}(Z^{(i-1)})), K_e < i \leq K_e + K_t, \quad (11)$$

where Bottleneck denotes the 2D convolutional layer with  $1 \times 1$  kernel and  $K_t$  is the number of blocks. The shape of input  $Z^{(i-1)}$  and output  $Z^{(i)}$  are  $(T, D, \hat{H}, \hat{W})$  and  $(\hat{T}, D, \hat{H}, \hat{W})$ , respectively.

**Decoder.** Finally, our decoder contains  $K_d$  unConvNormReLU blocks to output the final predictions  $\hat{Y}^{DST} = Z^{(K_e+K_t+K_d)}$ . In

**Table 1: Statistics of the datasets used in the experiments. The number of training and test sets of the dataset are  $N_{train}$  and  $N_{test}$  respectively, where the size of each image frame is  $(C, H, W)$ , and the length of the input and prediction sequences are  $T, K$  respectively.**

| Dataset     | $N_{train}$ | $N_{test}$ | $(C, H, W)$   | $T$ | $K$ |
|-------------|-------------|------------|---------------|-----|-----|
| MovingMNIST | 9000        | 1000       | (1, 64, 64)   | 10  | 10  |
| TrafficBJ   | 19627       | 1334       | (2, 32, 32)   | 4   | 4   |
| KTH         | 108717      | 4086       | (1, 128, 128) | 10  | 20  |
| SEVIR       | 4158        | 500        | (1, 384, 384) | 10  | 10  |
| RDS         | 2000        | 500        | (3, 128, 128) | 2   | 2   |
| EDPS        | 2000        | 500        | (3, 128, 128) | 2   | 2   |
| FS          | 2000        | 500        | (3, 128, 128) | 2   | 2   |

formulation, we have:

$$Z^{(i)} = \sigma \left( \operatorname{LayerNorm} \left( \operatorname{unConv2d} \left( Z^{(i-1)} \right) \right) \right), \quad (12)$$

$$K_e + K_t + 1 \leq i \leq K_e + K_t + K_d,$$

where unConv2d is implemented using ConvTranspose2d [12]. The shape of input  $Z^{(i-1)}$  and output  $Z^{(i)}$  are  $(\hat{T}, D, \hat{H}, \hat{W})$  and  $(T, C, H, W)$ , respectively.

### 3.4 Framework Summarization

Finally, we combine the output of both FPG and DST modules, which result in the final prediction:

$$\hat{Y}^{final} = \hat{Y}^{FPG} \oplus \hat{Y}^{DST}, \quad (13)$$

where  $\oplus$  represents element-wise addition. The whole framework would be optimizing by minimizing the vanilla MSE loss between the predictions and the target frame.

## 4 EXPERIMENT

### 4.1 Experimental Setups

**Datasets.** In this paper, the datasets studied can be classified into two categories from the perspective of PDE modeling or physics equation description: **Non-natural Phenomenon** datasets and **Natural Phenomenon** datasets. The former includes **MovingMNIST** [40], **TrafficBJ** [57], and **KTH** datasets [38]. Although they do not correspond to natural phenomena, the dynamic evolutionary processes expressed in these datasets can still be described by PDEs. The latter includes the **Storm Event ImagRy (SEVIR)** [42], **Reaction Diffusion System (RDS)**, **Elastic Double Pendulum System (EDPS)**, and **Fire System (FS)** datasets [6], which correspond to natural phenomena such as meteorology, chemical reactions, mechanical vibrations, and fire. These datasets are often used in the study of PDE modeling and the description of physics equations to better understand and predict the evolution of natural phenomena. We conduct experiments on seven datasets for evaluation. Here we summarize the details of the datasets used in this paper, The statistics are shown in the Table 1.

**Evaluation metrics.** We adopt Mean Squared Error (MSE), Mean Absolute Error (MAE), Multi-Scale Structural Similarity (MS-SSIM), Peak Signal-to-Noise Ratio (PSNR), and Learned Perceptual Image



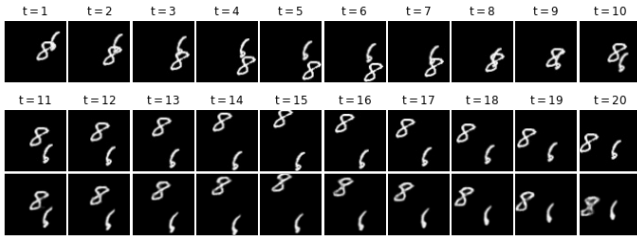


Figure 3: Example of prediction results for the Moving MNIST dataset. Top: input motion digital sequence; Middle: future real motion digital sequence; Bottom: PastNet predicted motion digital sequence.

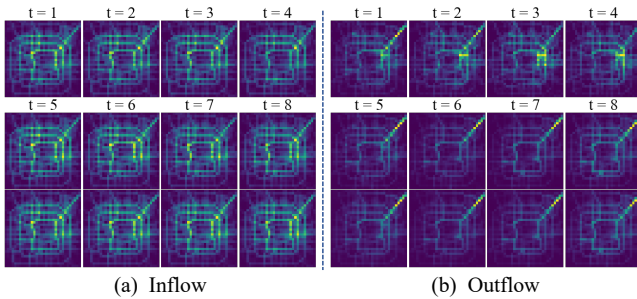


Figure 4: Example of prediction results on the TrafficBJ dataset. Top: input Traffic flow; Middle: future real Traffic flow; Bottom: PastNet predicted Traffic flow.

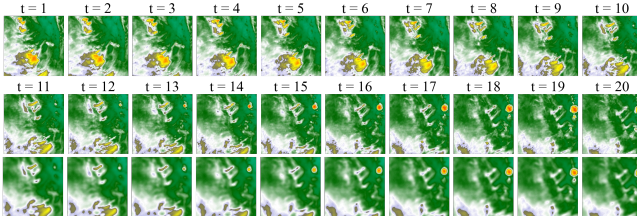


Figure 5: Example of prediction results on the SEVIR dataset. Top: input weather sequence; Middle: future real weather sequence; Bottom: PastNet predicted weather sequence.

Patch Similarity (LPIPS) to evaluate the quality of the predictions. Lower values of MSE, MAE, and LPIPS and higher values of SSIM and PSNR imply better performance.

**Implementation details.** The PastNet model features a consistent backbone architecture for all datasets, in which the FPG component is composed of 8-layer Fourier-based Spectral Filter. The DSM encoder incorporates 3-layer convolution block layers and 3-layer residual blocks, while the decoder utilizes 1-layer convolution block, 4-layer residual blocks, and 2-layer deconvolution blocks. All experiments in this paper were conducted on an NVIDIA A100-PCIE-40GB.

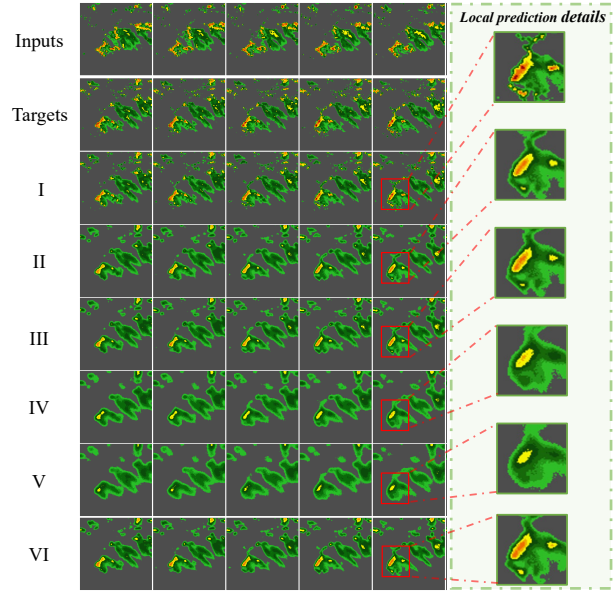


Figure 6: Inputs: The input weather sequences; Targets: The future real weather sequences; I: PastNet predicts the weather sequences; II: PastNet w/o FPG predicts the weather sequences; III: PastNet w/o FPG + UNet predicts the weather sequences; IV: PastNet w/o FPG + ViT predicts the weather sequences; V: PastNet w/o FPG + SwinT predicts the weather sequences; VI: PastNet w/o DST predicts the weather sequences.

## 4.2 Performance Comparison

We conduct a thorough evaluation of PastNet by comparing it with several baseline models on both non-natural and natural phenomena datasets. This includes competitive RNN architectures such as ConvLSTM [39], PredRNN-V1-2 [47], E3D LSTM [46], SA-ConvLSTM [25], PhyDnet [16], and MIM [48]. We also evaluate state-of-the-art CNN architecture SimVP [14] for non-natural phenomena datasets. For natural phenomenon datasets, we evaluate models that incorporate physical information, such as DLP [10], which uses an advection-diffusion flow model and achieves state-of-the-art performance on the SST dataset, it is commonly used for generic physical processes. We also evaluate NLDM [6], which combines manifold learning theory and autoencoder to discover fundamental variables hidden in physical experimental data for spatiotemporal prediction, as well as PhyDnet and SimVP. Our evaluation is meticulous to ensure the validity of the results.

Table 2 demonstrates that PastNet outperforms other models on non-natural phenomena datasets. Specifically, PastNet achieves the best MSE and MAE metrics on MovingMNIST, with values that are 20% and 10% lower than SimVP, respectively. Moreover, PastNet also achieves higher MS-SSIM and PSNR metrics than other models, indicating better prediction ability for dynamic changes in videos. On TrafficBJ, while PhyDnet has the best MSE and PSNR performance, PastNet comes in second place and achieves top spot for MAE and MS-SSIM. On KTH, PastNet achieves the best MSE and MAE performance, with values that are 33.6% and 35.8% lower than the second-place MIM model, respectively. Overall, PastNet

**Table 2: Quantitative prediction results of PastNet compared to Baselines on various Non-natural Phenomenon datasets. The evaluation metrics selected for this study are MSE ↓, MAE ↓, MS-SSIM ↑, and PSNR ↑, with a lower value (↓) indicating better performance for MSE and MAE, and a higher value (↑) indicating better performance for MS-SSIM and PSNR. The best result is indicated in boldface, while the second-best result is indicated with an underline in the table caption.**

| Method      | MovingMNIST  |              |               |              | TrafficBJ    |               |               |              | KTH          |              |               |              |
|-------------|--------------|--------------|---------------|--------------|--------------|---------------|---------------|--------------|--------------|--------------|---------------|--------------|
|             | MSE          | MAE          | MS-SSIM       | PSNR         | MSE x 100    | MAE           | MS-SSIM       | PSNR         | MSE          | MAE / 10     | MS-SSIM       | PSNR         |
| ConvLSTM    | 105.41       | 188.96       | 0.7498        | 26.27        | 48.45        | 18.921        | 0.9782        | 37.72        | 126.15       | 128.32       | 0.7123        | 23.58        |
| PredRNN-V1  | 81.87        | 147.31       | 0.8697        | 29.99        | 46.49        | 17.784        | 0.9789        | 38.11        | 101.52       | 99.21        | 0.8292        | 25.55        |
| E3D LSTM    | 67.25        | 136.99       | 0.8907        | 31.02        | 44.89        | 17.219        | 0.9731        | 38.71        | 86.17        | 85.55        | 0.8663        | 27.92        |
| SA-ConvLSTM | 79.76        | 142.21       | 0.8692        | 30.21        | 43.99        | 17.093        | 0.9672        | 38.98        | 89.35        | 87.20        | 0.8372        | 27.25        |
| PhyDnet     | 58.22        | 145.76       | 0.9012        | 32.13        | <b>42.21</b> | 16.975        | 0.9821        | <b>39.94</b> | 66.95        | 56.73        | 0.8831        | 28.02        |
| MIM         | 66.28        | 119.87       | 0.9017        | 31.12        | 43.98        | <u>16.645</u> | 0.9712        | 38.99        | 56.59        | 54.86        | 0.8666        | 28.97        |
| PredRNN-V2  | 48.42        | 126.18       | 0.8912        | 33.19        | 43.89        | 16.982        | 0.9723        | 39.02        | 51.15        | 50.64        | 0.8919        | 29.92        |
| SimVP       | <u>32.22</u> | <u>90.12</u> | <u>0.9371</u> | <u>37.17</u> | 43.32        | 16.897        | <u>0.9822</u> | 39.29        | <u>40.99</u> | <u>43.39</u> | <u>0.9061</u> | <u>33.72</u> |
| PastNet     | <b>31.77</b> | <b>89.33</b> | <b>0.9447</b> | <b>38.38</b> | <u>42.93</u> | <b>16.405</b> | <b>0.9876</b> | <u>39.42</u> | <b>33.83</b> | <b>35.26</b> | <b>0.9279</b> | <b>35.28</b> |

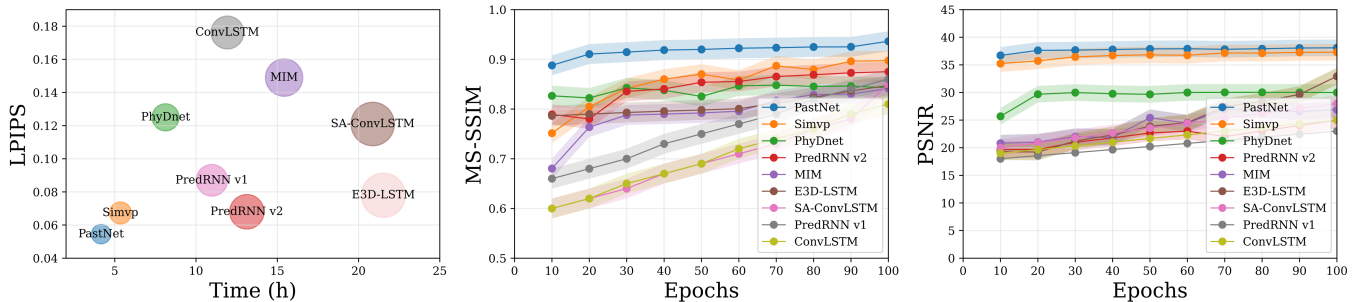


**Figure 7: PastNet outperforms other models in terms of efficiency and convergence rate on the MovingMNIST dataset. Specifically, it achieves the lowest LPIPS score in the shortest training time, as shown on the *Left* side of the figure. In addition, it achieves the highest MS-SSIM and PSNR scores within the same epochs, as depicted in the *Middle* and *Right* sides of the figure, respectively.**

shows significant advantages over other baseline methods in all evaluation metrics.

Results in Table 3 show that PastNet achieves the best performance in most evaluation metrics for all natural phenomena datasets. On the SEVIR dataset, PastNet achieves the lowest MSE and MAE scores, significantly better than other methods such as DLP, PhyDnet, and NLDM. On the RDS dataset, PastNet achieves the lowest MSE x 100 score, significantly better than other methods. On the EDPS dataset, PastNet achieves the highest MS-SSIM score, significantly better than SimVP. Overall, these results demonstrate that PastNet is highly effective in accurately predicting physical quantities and preserving structural information in various physical datasets, outperforming other state-of-the-art methods such as DLP, PhyDnet, NLDM, and SimVP.

We present the qualitative prediction results of PastNet for various datasets, highlighting its capability to accurately predict future images. Our findings demonstrate that PastNet can accurately predict numerical motions in MovingMNIST as depicted in Figure 3. Additionally, Figure 4 shows that PastNet reliably predicts traffic flow changes in the TrafficBJ dataset. Furthermore, PastNet performs well in the SEVIR weather dataset, as shown in Figure 5, where it accurately predicts high-resolution satellite images and

infers future weather changes. The visualization results for other datasets are available in the Appendix A.

### 4.3 Ablation Study

In this section, we demonstrate PastNet’s competitive performance on a wide range of datasets through a series of ablation studies. Table 4 and Figure 6 present the quantitative and qualitative results of these studies for different model structures, respectively. Specifically, **PastNet w/o FPG** removes the FPG module from the PastNet model. **PastNet w/o FPG + UNet** removes the FPG module from the PastNet model and uses UNet as an alternative module. **PastNet w/o FPG + ViT** removes the FPG module from the PastNet model and uses ViT as an alternative module. **PastNet w/o FPG + SwinT** removes the FPG module from the PastNet model and uses SwinT as an alternative module. **PastNet w/o DST** removes the DST module from the PastNet model. **PastNet** is the base PastNet model, which includes both the DST and FPG modules.

- PastNet outperforms other models with the lowest MSE, MAE, and highest SSIM, indicating its superior performance in video prediction.
- The inclusion of the DST module in PastNet improves the model’s training speed, making it a more efficient option.

**Table 3: Quantitative prediction results of PastNet compared to Baselines on various Natural Phenomenon datasets. The evaluation metrics selected for this study are MSE ↓, MAE ↓, MS-SSIM ↑, and PSNR ↑, with a lower value (↓) indicating better performance for MSE and MAE, and a higher value (↑) indicating better performance for MS-SSIM and PSNR. The best result is indicated in boldface, while the second-best result is indicated with an underline in the table caption.**

| Dataset | Model   | MSE          | MAE           | MS-SSIM       | PSNR         |
|---------|---------|--------------|---------------|---------------|--------------|
| SEVIR   | DLP     | 300.42       | 140.82        | 0.6772        | 36.59        |
|         | PhyDnet | 97.70        | 72.22         | 0.7137        | 43.03        |
|         | NLDM    | 295.93       | 170.73        | 0.6982        | 36.71        |
|         | SimVP   | <u>68.68</u> | <u>47.71</u>  | <u>0.7231</u> | <u>49.09</u> |
|         | PastNet | <b>66.13</b> | <b>44.84</b>  | <b>0.7568</b> | <b>49.78</b> |
| RDS     | DLP     | 1.38         | 2.08          | 0.9763        | 44.52        |
|         | PhyDnet | 0.51         | 1.25          | 0.9874        | 47.01        |
|         | NLDM    | 1.03         | 1.78          | 0.9594        | 46.56        |
|         | SimVP   | <u>0.15</u>  | <u>0.67</u>   | <u>0.9896</u> | <u>51.06</u> |
|         | PastNet | <b>0.13</b>  | <b>0.63</b>   | <b>0.9997</b> | <b>51.79</b> |
| EDPS    | DLP     | 3.53         | 281.82        | 0.9337        | 42.53        |
|         | PhyDnet | 1.08         | 167.23        | <u>0.9983</u> | 45.92        |
|         | NLDM    | 2.51         | 237.43        | 0.9455        | 42.83        |
|         | SimVP   | <b>0.93</b>  | <b>150.11</b> | 0.9882        | <b>46.25</b> |
|         | PastNet | <u>0.94</u>  | <u>168.53</u> | <b>0.9991</b> | <u>45.98</u> |
| FS      | DLP     | 7.78         | 426.12        | 0.9266        | 38.38        |
|         | PhyDnet | 4.41         | 327.32        | 0.9423        | 40.47        |
|         | NLDM    | 7.21         | 411.14        | 0.9392        | 38.62        |
|         | SimVP   | <u>3.01</u>  | <u>261.19</u> | <u>0.9647</u> | <u>42.03</u> |
|         | PastNet | <b>2.19</b>  | <b>222.08</b> | <b>0.9861</b> | <b>43.24</b> |

**Table 4: Experimental results of ablation with different model structures on the SEVIR dataset. The evaluation metrics selected for this study are MSE ↓, MAE ↓, MS-SSIM ↑, and Time(h) ↑, with a lower value (↓) indicating better performance for MSE, MAE and Time(h), and a higher value (↑) indicating better performance for MS-SSIM.**

| Model                   | MSE          | MAE          | SSIM        | Time (h)    |
|-------------------------|--------------|--------------|-------------|-------------|
| PastNet w/o FPG         | 133.8        | 103.6        | 0.67        | 3.19        |
| PastNet w/o FPG + UNet  | 115.4        | 99.35        | 0.61        | 16.54       |
| PastNet w/o FPG + ViT   | 287.3        | 139.5        | 0.49        | 23.87       |
| PastNet w/o FPG + SwinT | 321.8        | 158.7        | 0.54        | 24.12       |
| PastNet w/o DST         | 192.3        | 118.5        | 0.64        | 4.92        |
| PastNet                 | <b>73.21</b> | <b>52.31</b> | <b>0.74</b> | <b>4.16</b> |

- The FPG module is crucial for improving PastNet’s performance on the Natural Phenomenon dataset, with UNet as a potential alternative. This demonstrates PastNet’s versatility and ability to adapt to different datasets and tasks.

#### 4.4 Efficiency and Convergence Rate Analysis

Figure 7 on the left side clearly demonstrates the advantages of PastNet in terms of both time and LPIPS metrics. Notably, PastNet’s training time for 100 epochs is only 4.16 hours, considerably faster

**Table 5: Performance metrics for solving PDE equations using PastNet. The table shows the mean squared error (MSE), mean absolute error (MAE), and time per epoch (in seconds) for the Navier-Stokes equations (NSE) and Shallow-Water equations (SWE) in their 2D forms.**

| PDE | Evaluation Criterion |         |                    |
|-----|----------------------|---------|--------------------|
|     | MSE                  | MAE     | Time per epoch (s) |
| NSE | 0.3021               | 28.4952 | 218                |
| SWE | 0.0185               | 8.0391  | 223                |

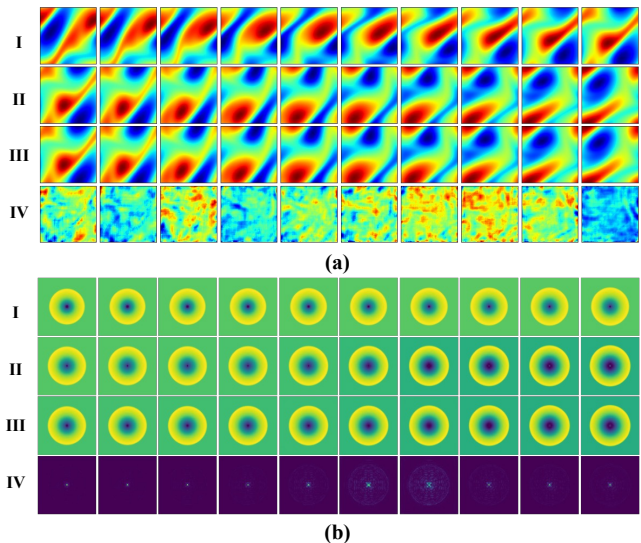


**Figure 8: (a) presents qualitative visualization results for NSE, while (b) displays the qualitative visualization results for SWE. The examples of the input PDE equations flow are denoted by  $I$ , examples of future PDE equations are denoted by  $II$ , predicted PDE equation examples are denoted by  $III$ , and the error between predicted and true results is denoted by  $IV$ , which is measured using the relative L2 error metric. Specifically, the relative L2 errors are calculated to be 0.0072 and 0.0007 for NSE and SWE, respectively. The formula for calculating the relative L2 error is given by  $\text{Relative L2 Error} = \frac{\|y - \hat{y}\|_2}{\|y - \bar{y}\|_2}$ , where  $y$  represents the true values,  $\hat{y}$  represents the predicted values,  $\bar{y}$  represents the mean of the true values, and  $\|\cdot\|_2$  denotes the L2 norm. These results suggest that the model is able to make accurate predictions, with a particularly low relative L2 error for SWE.**

than other models. Additionally, it achieves outstanding results in terms of LPIPS scores, indicating that PastNet can complete training more efficiently in a shorter amount of time while generating higher-quality images. The middle and right sides of Figure 7 illustrate the rapid improvement of PastNet in SSIM and PSNR metrics. Within approximately 60 epochs, PastNet achieves an SSIM metric of around 0.92, while other models remain below 0.85 at the same point. After 100 epochs, PastNet reaches a PSNR metric of approximately 38, which is far superior to other models. These results



highlight PastNet's superior convergence rate during training, enabling it to rapidly produce high-quality image results. In summary, PastNet is an accurate and efficient model for video prediction, with fast convergence and high-quality results. It represents a promising direction for future research and practical applications.

#### 4.5 Potential for Solving PDE Equations

To investigate the potential of PastNet for solving physical problems, we consider the Navier–Stokes equations, which represent viscous incompressible fluids in the form of vorticity on the unit torus, and the Shallow–Water equations, which are obtained from the general Navier–Stokes equations. We focus on their 2D forms, and more detailed descriptions of them are shown in Appendix B.

We use PastNet to solve the Navier–Stokes equations with viscosity  $\nu = 10^{-3}$  and a resolution of  $64 \times 64$  for training and testing. We use the flow field at 10 input time steps to predict the flow field at 10 future time steps ( $10_{timesteps} \mapsto 10_{timesteps}$ ). For the Shallow–Water equations, we fix the resolution to  $128 \times 128$  for training and testing and use the flow field at 50 input time steps to predict the flow field at 50 future time steps ( $50_{timesteps} \mapsto 50_{timesteps}$ ). We train for 200 epochs and record the metrics MSE, MAE, and the time per epoch. The quantitative and qualitative results are presented in Table 5 and Figure 8, respectively.

The results in Table 5 indicate that PastNet has potential for solving PDE equations, especially for the SWE equation, as it achieved lower MSE and MAE values for the SWE equation than for the NSE equation, while the time per epoch was similar for both equations.

## 5 CONCLUSION

In this paper, we investigate the problem of spatio-temporal video prediction and propose a novel method named PastNet to tackle the problem. The key insight of our PastNet is to incorporate a spectral convolution operator in the Fourier domain, which effectively introduces inductive biases from the underlying physical laws. Moreover, we introduce both local feature discretization and intrinsic dimensionality estimation to reduce the computational costs with accuracy retained. Extensive experiments on a range of popular datasets show that the proposed PastNet is more effective and efficient than state-of-the-art techniques. In future works, we would develop more effective video prediction techniques by introducing high-level physical domain knowledge in various fields.

## REFERENCES

- [1] Mohammad Babaeizadeh, Chelsea Finn, Dumitru Erhan, Roy H Campbell, and Sergey Levine. 2017. Stochastic variational video prediction. In *Proceedings of the International Conference on Learning Representations*.
- [2] Xinzhu Bei, Yanchao Yang, and Stefano Soatto. 2021. Learning semantic-aware dynamics for video prediction. In *Proceedings of the IEEE/CVF Conference on Computer Vision and Pattern Recognition*. 902–912.
- [3] Michael M Bronstein, Joan Bruna, Yann LeCun, Arthur Szlam, and Pierre Vandergheynst. 2017. Geometric deep learning: going beyond euclidean data. *IEEE Signal Processing Magazine* 34, 4 (2017), 18–42.
- [4] Zhangjie Cao, Mingsheng Long, Jianmin Wang, and Philip S Yu. 2017. Hashnet: Deep learning to hash by continuation. In *Proceedings of the IEEE/CVF International Conference on Computer Vision*. 5608–5617.
- [5] Zheng Chang, Xinfeng Zhang, Shanshe Wang, Siwei Ma, and Wen Gao. 2022. Strpm: A spatiotemporal residual predictive model for high-resolution video prediction. In *Proceedings of the IEEE/CVF Conference on Computer Vision and Pattern Recognition*. 13946–13955.
- [6] Boyuan Chen, Kuang Huang, Sunand Raghupathi, Ishaan Chandratreya, Qiang Du, and Hod Lipson. 2022. Automated discovery of fundamental variables hidden in experimental data. *Nature Computational Science* 2, 7 (2022), 433–442.
- [7] Xiongtao Chen and Wenmin Wang. 2019. Uni-and-bi-directional video prediction via learning object-centric transformation. *IEEE Transactions on Multimedia* 22, 6 (2019), 1591–1604.
- [8] Changmao Cheng, Chi Zhang, Yichen Wei, and Yu-Gang Jiang. 2019. Sparse temporal causal convolution for efficient action modeling. In *Proceedings of the ACM International Conference on Multimedia*. 592–600.
- [9] Taco Cohen, Maurice Weiler, Berkay Kicanaoglu, and Max Welling. 2019. Gauge equivariant convolutional networks and the icosahedral CNN. In *Proceedings of the International Conference on Machine Learning*. 1321–1330.
- [10] Emmanuel de Bezenac, Arthur Pajot, and Patrick Gallinari. [n.d.]. Deep Learning for Physical Processes: Incorporating Prior Scientific Knowledge. In *International Conference on Learning Representations*.
- [11] Alexey Dosovitskiy, Lucas Beyer, Alexander Dehghani, Dirk Weissenborn, Xi-aohua Zhai, Thomas Unterthiner, Mostafa Dehghani, Matthias Minderer, Georg Heigold, Sylvain Gelly, et al. 2020. An image is worth 16x16 words: Transformers for image recognition at scale. *arXiv preprint arXiv:2010.11929* (2020).
- [12] Vincent Dumoulin and Francesco Visin. 2016. A guide to convolution arithmetic for deep learning. *arXiv preprint arXiv:1603.07285* (2016).
- [13] Jean-Yves Franceschi, Edouard Delasalles, Mickaël Chen, Sylvain Lamprier, and Patrick Gallinari. 2020. Stochastic latent residual video prediction. In *Proceedings of the International Conference on Machine Learning*. 3233–3246.
- [14] Zhangyang Gao, Cheng Tan, Lirong Wu, and Stan Z Li. 2022. Simvp: Simpler yet better video prediction. In *Proceedings of the IEEE/CVF Conference on Computer Vision and Pattern Recognition*. 3170–3180.
- [15] Nicholas Geneva and Nicholas Zabarar. 2020. Modeling the dynamics of PDE systems with physics-constrained deep auto-regressive networks. *J. Comput. Phys.* 403 (2020), 109056.
- [16] Vincent Le Guen and Nicolas Thome. 2020. Disentangling physical dynamics from unknown factors for unsupervised video prediction. In *Proceedings of the IEEE/CVF Conference on Computer Vision and Pattern Recognition*. 11474–11484.
- [17] John Guibas, Morteza Mardani, Zongyi Li, Andrew Tao, Anima Anandkumar, and Bryan Catanzaro. 2021. Adaptive fourier neural operators: Efficient token mixers for transformers. *arXiv preprint arXiv:2111.13587* (2021).
- [18] John Guibas, Morteza Mardani, Zongyi Li, Andrew Tao, Anima Anandkumar, and Bryan Catanzaro. 2021. Efficient Token Mixing for Transformers via Adaptive Fourier Neural Operators. In *International Conference on Learning Representations*.
- [19] Qiyu Hu, Guangyi Zhang, Zhijin Qin, Yunlong Cai, Guanding Yu, and Geoffrey Ye Li. 2023. Robust semantic communications with masked VQ-VAE enabled codebook. *IEEE Transactions on Wireless Communications* (2023).
- [20] Xiaotao Hu, Zhewei Huang, Ailin Huang, Jun Xu, and Shuchang Zhou. 2023. A Dynamic Multi-Scale Voxel Flow Network for Video Prediction. In *Proceedings of the IEEE/CVF Conference on Computer Vision and Pattern Recognition*.
- [21] George Em Karniadakis, Ioannis G Kevrekidis, Lu Lu, Paris Perdikaris, Sifan Wang, and Liu Yang. 2021. Physics-informed machine learning. *Nature Reviews Physics* 3, 6 (2021), 422–440.
- [22] Wonkwang Lee, Whie Jung, Han Zhang, Ting Chen, Jing Yu Koh, Thomas Huang, Hyungsuk Yoon, Honglak Lee, and Seunghoon Hong. 2021. Revisiting hierarchical approach for persistent long-term video prediction. In *Proceedings of the International Conference on Learning Representations*.
- [23] Elizaveta Levina and Peter Bickel. 2004. Maximum likelihood estimation of intrinsic dimension. In *Proceedings of the Conference on Neural Information Processing Systems*.
- [24] Zongyi Li, Nikola Kovachki, Kamyar Aizzadenesheli, Burigede Liu, Kaushik Bhattacharya, Andrew Stuart, and Anima Anandkumar. 2020. Fourier neural operator for parametric partial differential equations. In *Proceedings of the International Conference on Learning Representations*.
- [25] Zhihui Lin, Maomao Li, Zhuobin Zheng, Yangyang Cheng, and Chun Yuan. 2020. Self-attention convlstm for spatiotemporal prediction. In *Proceedings of the AAAI conference on artificial intelligence*, Vol. 34. 11531–11538.
- [26] Dachuan Liu, Jin Wang, Shuo Shang, and Peng Han. 2022. Msdr: Multi-step dependency relation networks for spatial temporal forecasting. In *Proceedings of the International ACM SIGKDD Conference on Knowledge Discovery & Data Mining*. 1042–1050.
- [27] Ziwei Liu, Raymond A Yeh, Xiaoou Tang, Yiming Liu, and Aseem Agarwala. 2017. Video frame synthesis using deep voxel flow. In *Proceedings of the IEEE/CVF International Conference on Computer Vision*. 4463–4471.
- [28] Zichao Long, Yiping Lu, Xianzhong Ma, and Bin Dong. 2018. Pde-net: Learning pdes from data. In *Proceedings of the International Conference on Machine Learning*. 3208–3216.
- [29] William Lotter, Gabriel Kreiman, and David Cox. 2017. Deep predictive coding networks for video prediction and unsupervised learning. In *Proceedings of the International Conference on Learning Representations*.
- [30] Lu Lu, Pengzhan Jin, Guofei Pang, Zhongqiang Zhang, and George Em Karniadakis. 2021. Learning nonlinear operators via DeepONet based on the universal approximation theorem of operators. *Nature Machine Intelligence* 3, 3 (2021), 218–229.

- [31] Stanislav Morozov and Artem Babenko. 2019. Unsupervised neural quantization for compressed-domain similarity search. In *Proceedings of the IEEE/CVF International Conference on Computer Vision*. 3036–3045.
- [32] Junting Pan, Chengyu Wang, Xu Jia, Jing Shao, Lu Sheng, Junjie Yan, and Xiaogang Wang. 2019. Video generation from single semantic label map. In *Proceedings of the IEEE/CVF Conference on Computer Vision and Pattern Recognition*. 3733–3742.
- [33] Jialun Peng, Dong Liu, Songcen Xu, and Houqiang Li. 2021. Generating diverse structure for image inpainting with hierarchical VQ-VAE. In *Proceedings of the IEEE/CVF Conference on Computer Vision and Pattern Recognition*. 10775–10784.
- [34] Maziar Raissi. 2018. Deep hidden physics models: Deep learning of nonlinear partial differential equations. *Journal of Machine Learning Research* 19, 1 (2018), 932–955.
- [35] Maziar Raissi, Paris Perdikaris, and George E Karniadakis. 2019. Physics-informed neural networks: A deep learning framework for solving forward and inverse problems involving nonlinear partial differential equations. *Journal of Computational physics* 378 (2019), 686–707.
- [36] René Ranftl, Alexey Bochkovskiy, and Vladlen Koltun. 2021. Vision transformers for dense prediction. In *Proceedings of the IEEE/CVF International Conference on Computer Vision*. 12179–12188.
- [37] Yongming Rao, Wenliang Zhao, Benlin Liu, Jiwen Lu, Jie Zhou, and Cho-Jui Hsieh. 2021. Dynamicvit: Efficient vision transformers with dynamic token sparsification. (2021), 13937–13949.
- [38] C. Schuldt, I. Laptev, and B. Caputo. 2004. Recognizing human actions: a local SVM approach. In *Proceedings of the 17th International Conference on Pattern Recognition, 2004. ICPR 2004.*, Vol. 3. 32–36 Vol.3. <https://doi.org/10.1109/ICPR.2004.1334462>
- [39] Xingjian Shi, Zhourong Chen, Hao Wang, Dit-Yan Yeung, Wai-Kin Wong, and Wang-chun Woo. 2015. Convolutional LSTM network: A machine learning approach for precipitation nowcasting. In *Proceedings of the Conference on Neural Information Processing Systems*.
- [40] Nitish Srivastava, Elman Mansimov, and Ruslan Salakhutdinov. 2015. Unsupervised Learning of Video Representations Using LSTMs. In *Proceedings of the 32nd International Conference on International Conference on Machine Learning - Volume 37 (Lille, France) (ICML '15)*. JMLR.org, 843–852.
- [41] Aaron Van Den Oord, Oriol Vinyals, et al. 2017. Neural discrete representation learning. In *Proceedings of the Conference on Neural Information Processing Systems*.
- [42] Mark Veillette, Siddharth Samsi, and Chris Mattioli. 2020. Sevir: A storm event imagery dataset for deep learning applications in radar and satellite meteorology. *Advances in Neural Information Processing Systems* 33 (2020), 22009–22019.
- [43] Ruben Villegas, Arkanath Pathak, Harini Kannan, Dumitru Erhan, Quoc V Le, and Honglak Lee. 2019. High fidelity video prediction with large stochastic recurrent neural networks. In *Proceedings of the Conference on Neural Information Processing Systems*.
- [44] Ruben Villegas, Jimei Yang, Seunghoon Hong, Xunyu Lin, and Honglak Lee. 2017. Decomposing motion and content for natural video sequence prediction. In *Proceedings of the International Conference on Learning Representations*.
- [45] Ting-Chun Wang, Ming-Yu Liu, Jun-Yan Zhu, Guilin Liu, Andrew Tao, Jan Kautz, and Bryan Catanzaro. 2018. Video-to-video synthesis. In *Proceedings of the Conference on Neural Information Processing Systems*.
- [46] Yunbo Wang, Lu Jiang, Ming-Hsuan Yang, Li-Jia Li, Mingsheng Long, and Li Fei-Fei. 2019. Eidetic 3d lstm: A model for video prediction and beyond. In *International conference on learning representations*.
- [47] Yunbo Wang, Haixu Wu, Jianjin Zhang, Zhifeng Gao, Jianmin Wang, S Yu Philip, and Mingsheng Long. 2022. Predrnn: A recurrent neural network for spatiotemporal predictive learning. *IEEE Transactions on Pattern Analysis and Machine Intelligence* 45, 2 (2022), 2208–2225.
- [48] Yunbo Wang, Jianjin Zhang, Hongyu Zhu, Mingsheng Long, Jianmin Wang, and Philip S Yu. 2019. Memory in memory: A predictive neural network for learning higher-order non-stationarity from spatiotemporal dynamics. In *Proceedings of the IEEE/CVF Conference on Computer Vision and Pattern Recognition*. 9154–9162.
- [49] Haixu Wu, Zhiyu Yao, Jianmin Wang, and Mingsheng Long. 2021. MotionRNN: A flexible model for video prediction with spacetime-varying motions. In *Proceedings of the IEEE/CVF Conference on Computer Vision and Pattern Recognition*. 15435–15444.
- [50] Yue Wu, Rongrong Gao, Jaesik Park, and Qifeng Chen. 2020. Future video synthesis with object motion prediction. In *Proceedings of the IEEE/CVF Conference on Computer Vision and Pattern Recognition*. 5539–5548.
- [51] Yue Wu, Qiang Wen, and Qifeng Chen. 2022. Optimizing video prediction via video frame interpolation. In *Proceedings of the IEEE/CVF Conference on Computer Vision and Pattern Recognition*. 17814–17823.
- [52] Jingwei Xu, Huaazhe Xu, Bingbing Ni, Xiaokang Yang, and Trevor Darrell. 2020. Video prediction via example guidance. In *Proceedings of the International Conference on Machine Learning*. 10628–10637.
- [53] Yechao Xu, Zhengxing Sun, Qian Li, Yunhan Sun, and Shoutong Luo. 2022. Active Patterns Perceived for Stochastic Video Prediction. In *Proceedings of the ACM International Conference on Multimedia*. 5961–5969.
- [54] Wilson Yan, Yunzhi Zhang, Pieter Abbeel, and Aravind Srinivas. 2021. Videogpt: Video generation using vq-vae and transformers. *arXiv preprint arXiv:2104.10157* (2021).
- [55] Yibo Yang and Paris Perdikaris. 2019. Conditional deep surrogate models for stochastic, high-dimensional, and multi-fidelity systems. *Computational Mechanics* 64 (2019), 417–434.
- [56] Xi Ye and Guillaume-Alexandre Bilodeau. 2022. VPTR: Efficient Transformers for Video Prediction. In *International Conference on Pattern Recognition*. 3492–3499.
- [57] Junbo Zhang, Yu Zheng, and Dekang Qi. 2017. Deep spatio-temporal residual networks for citywide crowd flows prediction. In *Proceedings of the AAAI conference on artificial intelligence*, Vol. 31.
- [58] Tiesong Zhao, Yuhang Huang, Weize Feng, Yiwen Xu, and Sam Kwong. 2022. Efficient VVC Intra Prediction Based on Deep Feature Fusion and Probability Estimation. *IEEE Transactions on Multimedia* (2022).
- [59] Xiaosu Zhu, Jingkuan Song, Lianli Gao, Xiaoyan Gu, and Heng Tao Shen. 2023. Revisiting Multi-Codebook Quantization. *IEEE Transactions on Image Processing* (2023).

## APPENDIX

### A VISUAL PRESENTATION OF PREDICTION RESULTS

The visualization results for the other datasets are shown below: Figure9 demonstrates PastNet's proficiency in the KTH pedestrian motion dataset, accurately predicting future pedestrian trajectories; Finally, Figure10 illustrates PastNet's capability in predicting the systematic evolution of physical dynamics datasets such as RDS, EDPS, and FS.

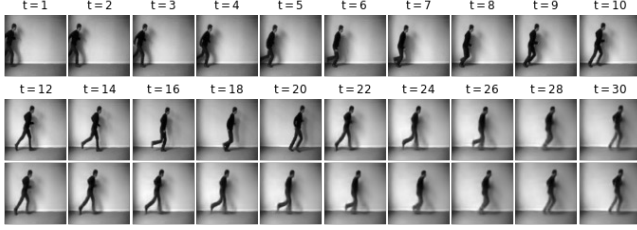


**Figure 9: Example of prediction results on the KTH dataset. Top: input Pedestrian movement sequence; Middle: future real Pedestrian movement sequence; Bottom: PastNet predicted Pedestrian movement sequence.**

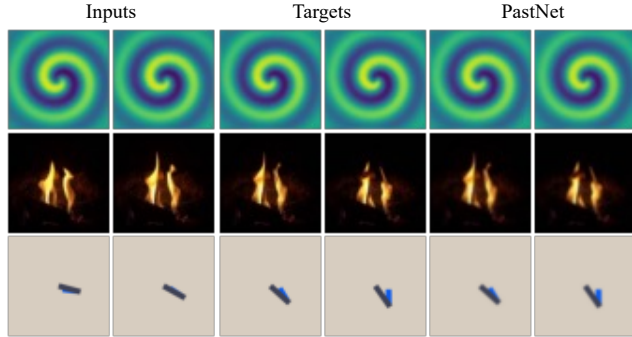


**Figure 10: Examples of prediction results on the Reaction Diffusion System, Elastic Double Pendulum System and Fire System datasets; two input frames predict two output frames; from left to right, the input sequence, the target sequence and the PastNet prediction sequence.**

## B DESCRIPTION OF THE DETAILS OF THE PDE EQUATIONS

### B.1 2D Navier-Stokes Equations

This paper considers the 2D Navier-Stokes equations for a viscous, incompressible fluid with vorticity in the form of a curl on the unit torus.

$$\begin{aligned} \partial_t w(x, t) + u(x, t) \cdot \nabla w(x, t) &= \nu \Delta w(x, t) + f(x) & x \in (0, 1)^2, t \in (0, T] \\ \nabla \cdot u(x, t) &= 0, & x \in (0, 1)^2, t \in [0, T] \\ w(x, 0) &= w_0(x), & x \in (0, 1)^2 \end{aligned} \quad (14)$$

In this context,  $u \in C([0, T]; H_r^{per}((0, 1)^2; \mathbb{R}^2))$  for any  $r > 0$  is the velocity field,  $w = \nabla \times u$  is the vorticity,  $w_0 \in L_{per}^2((0, 1)^2; \mathbb{R})$  is the initial vorticity,  $\nu \in \mathbb{R}^+$  is the viscosity coefficient, and  $f \in L_{per}^2((0, 1)^2; \mathbb{R})$  is the forcing function. The time evolution of the equation is visualized in Figure 11.

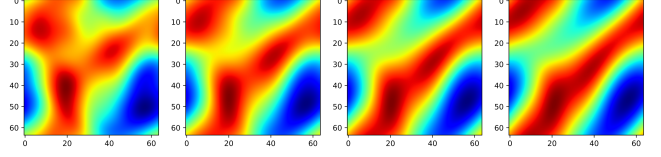


**Figure 11: This visualization concerns the time evolution of data generated by the 2D Navier-Stokes equations.**

### B.2 2D Shallow-Water Equations

The Navier-Stokes equations are the fundamental equations that describe viscous flow in fluid mechanics. The shallow water equations can be derived from the Navier-Stokes equations and are used to model free-surface flow problems. In two dimensions, these equations can be expressed as a system of hyperbolic partial differential equations.

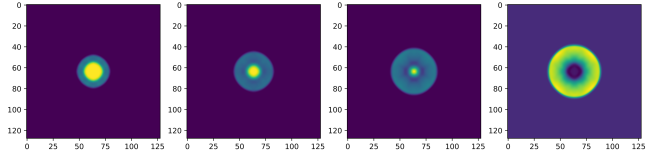


**Figure 12: This visualization concerns the time evolution of data generated by the 2D shallow water equations.**

$$\partial_t h + \partial_x hu + \partial_y hv = 0 \quad (15)$$

$$\partial_t hu + \partial_x \left( u^2 h + \frac{1}{2} g_r h^2 \right) = -g_r h \partial_x b \quad (16)$$

$$\partial_t hv + \partial_y \left( v^2 h + \frac{1}{2} g_r h^2 \right) = -g_r h \partial_y b \quad (17)$$

In the shallow water equations, which are used to model free-surface flow problems,  $u$  and  $v$  represent the horizontal and vertical velocities,  $h$  represents the water depth, and  $b$  describes the spatial variation of the depth. The terms  $hu$  and  $hv$  can be interpreted as the directional momentum components, and  $g$  represents the acceleration due to gravity.

The benchmark for the shallow water equation problem presented in Subsection 4.5 includes a specific simulation of a two-dimensional radial dam-breaking scheme. The simulation takes place on a square domain  $\Omega = [-2.5, 2.5]^2$ , where the initial water height is represented by a circular bulge at the center of the domain.

$$h(t=0, x, y) = \begin{cases} 2.0, & \text{for } r < \sqrt{x^2 + y^2} \\ 1.0, & \text{for } r \geq \sqrt{x^2 + y^2} \end{cases} \quad (18)$$

The time evolution of the equation is visualized in Figure 12.